

# Thermoelectric modeling of the ATLAS ITk Strip Detector

Kurt Brendlinger<sup>1</sup>, Georg Viehhauser<sup>1</sup>, Graham Beck<sup>1</sup>, Yu-Heng Chen<sup>1</sup>

---

## Abstract

Here is the abstract.

*Keywords:* Silicon detector, Thermal runaway, Thermal management, Cooling

---

## 1. Introduction

The temperatures in silicon detector systems are critically important to the performance of these systems. The leakage current shows a pronounced temperature dependence

$$I \propto T_S^2 e^{-T_A/T_S} \quad (1)$$

where  $T_S$  is the sensor temperature and  $T_A \simeq 7000$  K. Leakage currents can become particularly significant after irradiation of the silicon material. The heat generated by these leakage currents in the silicon sensor, together with the heat from front-end electronics components on the detector needs to be removed by cooling systems. Due to the strong growth of leakage power with temperature there is a critical temperature  $T_C$ , above which the heat cannot be removed quickly enough, and the detector becomes thermally unstable ('thermal runaway'). The capability of the cooling system in removing this heat is limited by the temperature of the local cold sink (typically the coolant temperature) and the thermal impedance of the heat path between the source (electronics and sensor) and the sink.

In addition, there can be aspects of the front-end electronics which are temperature-dependent. For example, in the strip system for the ATLAS phase II upgrade (ref) there are two additional sources for temperature-dependent heat sources. The first is a radiation damage effect in the digital part of the readout-electronics (the ABC130 and HCC chips), which is manufactured in 130 nm technology by the xxx process (ref). This effect leads to a scaling of the digital power in the chip depending on the received dose rate (TID) and the temperature of the chip (ref). This has been first observed in the ATLAS IBL (ref). The other temperature dependence of the power generated by the front-end electronics stems from the temperature dependence of the converter chip (FEAST (ref)) used in the on-detector DC-DC converter system supplying power to the front-end electronics.

Even before the limit of thermal stability is reached, knowledge of temperatures in silicon detector systems is important, as they define system parameters like power supply capacity and cable dimensions.

In principle the temperatures in the system for a given set of operational parameters (power density, thermal conductivities etc.) can be predicted by FEA to an accuracy which is given by the quality of the input parameters. However, this is a time-consuming process and can be prohibitively difficult if there is a number of local heat sources depending non-linearly on the temperature. A simplification to this problem which allows for an analytical solution in the case of a simple heat source topology has been developed in [1]. Here we develop this method further to include several temperature dependent non-linear heat sources in the front-end electronics. The resulting set of equations cannot be solved analytically any more, but with little effort using numerical problem solvers. This enables us to predict with some confidence the temperatures and power requirements in the ATLAS strip system throughout phase II operation. The results from this prediction have been used throughout the project to consistently dimension the different systems (cooling, power, services etc.) also with some robustness due to the inclusion of a common set of safety factors. This method can be easily adapted to any other system after adjustment of the system specific geometries and parameters.

### 1.1. The ATLAS strip system

The strip system for the ATLAS phase II upgrade (ref TDR) consists of two parts: the barrel system comprised of four concentric cylindrical barrels and the two endcaps, which consist of six disks each.

In the barrel the detector modules are made of square sensors ( $96.85 \times 96.72 \text{ mm}^2$ ) with a hybrid on top, which hosts the front-end chips (ABC\* and HCC\*), but also circuitry to convert the supply voltage of larger than 10 V to the chip voltage of 1.5 V. This circuitry is controlled by the FEAST chip. The modules are glued onto both sides of a composite sandwich which contains two parallel thin wall titanium cooling pipes embedded in carbon foam (Allcomp K9 - ref) between two facesheets of UHM carbon fibre (3 layers of K13C2U/EX1515) with a co-cured Kapton/copper low-mass tape. A model of this geometry is shown in fig. 1. During final operation cooling will be achieved by evaporating CO<sub>2</sub> in the cooling pipes with a final target temperature of not higher than -35°C anywhere on the stave. With the exception of the end region of the stave, where a side-mounted End-Of-Structure (EOS) card is located and the thermal path is degraded by the presence of electrically insulating ceramic pipe sections, the geometry of the stave is uniform along its length.

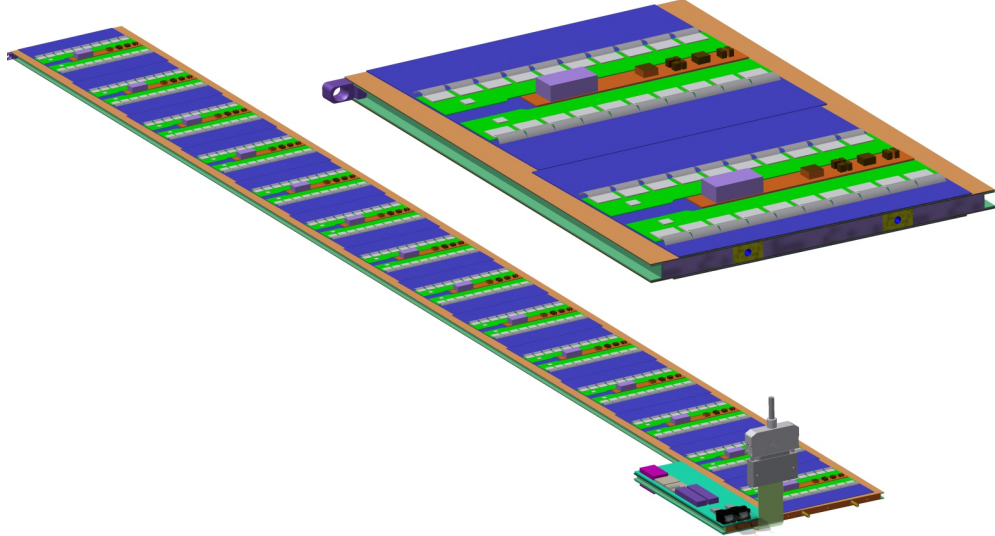


Figure 1: Strip barrel local support geometry. On the left a complete stave is shown (note the end-of-structure card in the foreground). The right picture shows a detailed cross-section through the stave with the two cooling pipes visible inside the core.

The endcap detector consists of six disks, each containing 32 “petals” loaded on both sides with six silicon modules (twelve total). The endcap detector modules consist of six distinct designs located at increasing radius from the beam pipe and labeled R0 through R5 (where “R” stands for ring). Each endcap module consists of one or two irregularly-shaped silicon sensors, and a varying number of front-end chips on each module (between 12 and 28 ABCs, and 2 to 4 HCCs). The EOS card is located adjacent to the R5 module, but the cooling pipes (and not the electrical breaks) run directly underneath it, in contrast to the barrel EOS. The remaining module and petal core design details are largely identical to the barrel module description above. Fig. 2 depicts the geometry of the endcap petal.

Figure 2: Endcap strip geometry

### 1.2. Radiation environment

A key input to the calculation is the radiation environment of the strip system, as several inputs depend on radiation damage effects. The sensor leakage current is a function of the fluence expressed in 1 MeV

neutron-equivalents, and the TID effect on the digital chip current will be parametrized as a function of the total ionizing dose rate (more details on its dependencies can be found in section xxx).

As can be seen in figure 3, both of these quantities display a weak dependence on  $z$  in the barrel, whereas they vary significantly along  $r$  over the length of the endcap petals. Because of this, and the linear uniformity of the stave compared to the more complex geometry along a petal, we modelled only two types of modules for the barrel (a generic module along the linear part of the stave and the module next to the end-of-structure card), but six different types of modules in a petal.

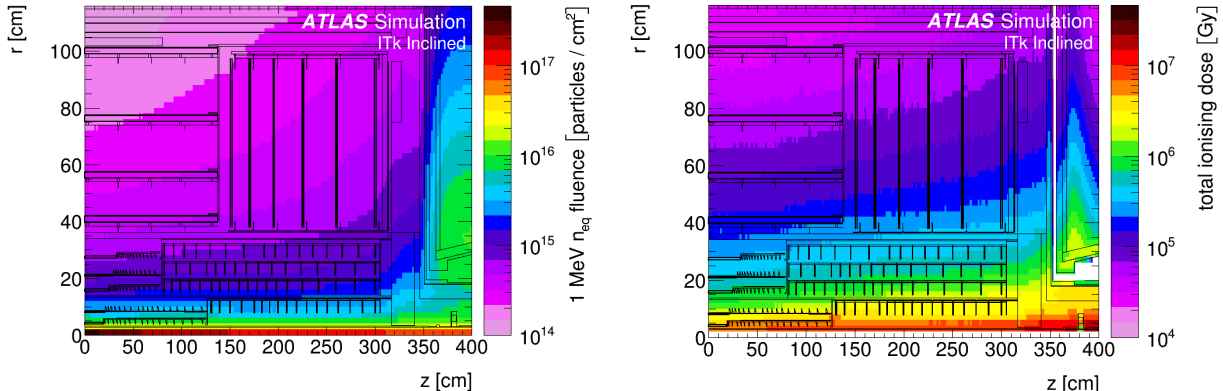


Figure 3: ATLAS ITk radiation environment. 1 MeV neutron equivalent fluence (left) and total ionizing dose (right). Both plots are for an integrated luminosity of  $4000 \text{ fb}^{-1}$  (ref strip TDR).

## 2. The electrical model

The electrical model consists of low-voltage (LV) and high-voltage (HV) circuits, depicted in Fig. 4. The LV current is used to power the hybrid controller chips (HCCs), ATLAS Binary Chips (ABCs) and Autonomous Monitoring and Control chip (AMAC) located on PCBs that are glued directly onto the surface of the sensor. The number of chips vary according to the design of each different module type (barrel short-strip and long-strip modules, and six different endcap module designs).

The ABCs and HCCs are all powered at 1.5 V using a DCDC converter (the FEAST) to step the voltage down from 11 V. Typically one FEAST is used per module is used to power the chips; however, due to the large number of ABCs on endcap module R3, the load is split across two FEAST converters.

The AMAC contains a component powered at 1.5 V and one powered at 3 V; both are delivered from the 11 V source by an LDO regulator with a 1.9 mA quiescent current. Again, the endcap module R3 differs from other modules, containing two AMACs each powered by its own LDO.

The bus tape, which carries both LV and HV currents, is expected to emit some heat due to the wire resistance. This impacts the module in two ways: first, the tape itself will radiate some heat according to the amount of current passing through it; this source of heat is accounted for in the model, however the contribution to the total power of the module is negligible. Second, the voltage supplied to the module will be affected by the small  $\Delta V$  in the bus tape. This effect is largest for modules on the non-EOS end of the barrel stave or endcap petal, where the current has traveled a longer distance. The treatment of this effect is slightly different in the barrel and endcap models: in the barrel, the voltage delivered to every module is set at 10.5 V; in the endcap, the  $\Delta V$  is estimated based on the calculated expected power loss along the tape for each module. In both cases, the effect of different treatment is small.

The low-voltage current is also delivered to the EOS card to power various data transfer components, which require 2.5 V and 1.2 V currents. On the EOS, a FEAST identical to the one used on the module is used to step the voltage down from 11 V to 2.5 V; an additional LDO regulator brings 2.5 V down to 1.2 V for some components.

Finally, the HV current is used to provide the voltage bias on the silicon sensors. An HV multiplexer switch (HVMUX) is placed in parallel to the sensor, which can be used to disconnect the sensor from the bias line. Two HV filters with an effective resistance of  $10 \text{ k}\Omega$  are placed in series with the sensor. The nominal

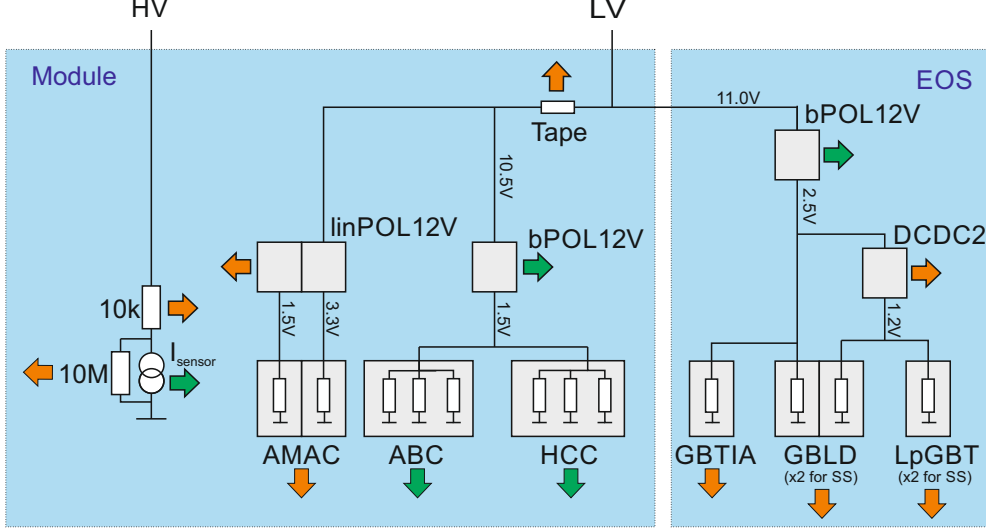


Figure 4: The electrical model of the ITk Strip barrel and endcap modules. Green arrows represent temperature-dependent heat sources, while orange arrows are temperature-independent. Grey squares are chips. Chip counts per module are linPOL12V/bPOL12V/AMAC: 1 each (2 each for EC R3); HCC: 1 for barrel LS, 2 for barrel SS and EC R0-R2 and R4-R5, 4 for EC R3; ABC: barrel: 10, 20 (LS, SS), EC: 17, 21, 21, 28, 16, 18 (R0-R5).

operating voltage of the sensor is expected to be 500V, but the system is designed to operate with a voltage bias of up to 700V.

### 3. The thermal model

The thermal network consists of heat sources (some of which are temperature dependent) and thermal resistances. The latter are given by the properties of the mechanical design (heat conductivities of the materials) and the geometry of the heat path. The geometry is generally 3-dimensional, but it is the strategy of the simple network models to lump the 3-dimensional behaviour into one thermal resistance parameter. In the models discussed here we have used a granularity corresponding to single detector modules for which the thermal resistance has been modelled. The temperatures in the model are then given for the nodes in the network in analogy to the potentials in an electrical network.

The complexity of the thermal network used in this study (see figure 5) is given by the variety of different temperature-dependent heat sources in the ATLAS strip system. In addition to the sensor leakage currents these are the digital power for each type of chip, and the heat generated by the FEAST chip, which is providing the DC-DC conversion on the detector. In the ATLAS SCT modules all these components are located on top of the sensors, so that the heat generated in them flows through the sensor into the support structure, the stave (barrel) or petal (endcap) core with the embedded cooling pipe. In the network model the heat flow from these sources is combined and flowing through a common impedance  $R_M$  to the sink at a temperature  $T_C$ . For each of the temperature-dependent heat sources (ABC, HCC, FEAST and the sensor) we have added a resistance from the common temperature  $T_{mod}$  to allow for a finite and different heat path for each of them. Finally, in the case of the barrel system, there is an additional source of heat for the last module on the stave, which is the adjacent End-of-substructure (EOS) card, which is modeled by an additional source with an impedance for its special heat path.

This is a more complex thermal network than the one studied in ref. [1], where an analytical solution for the determination of thermal stability was given. In particular because of the non-linear temperature dependence of some of the heat sources it is not possible any more to solve the set of equations describing the model here analytically. However, the set of equations is still sufficiently small to solve it numerically using readily available functions in Mathematica (used in the barrel model) or xxx (used in the endcap system).

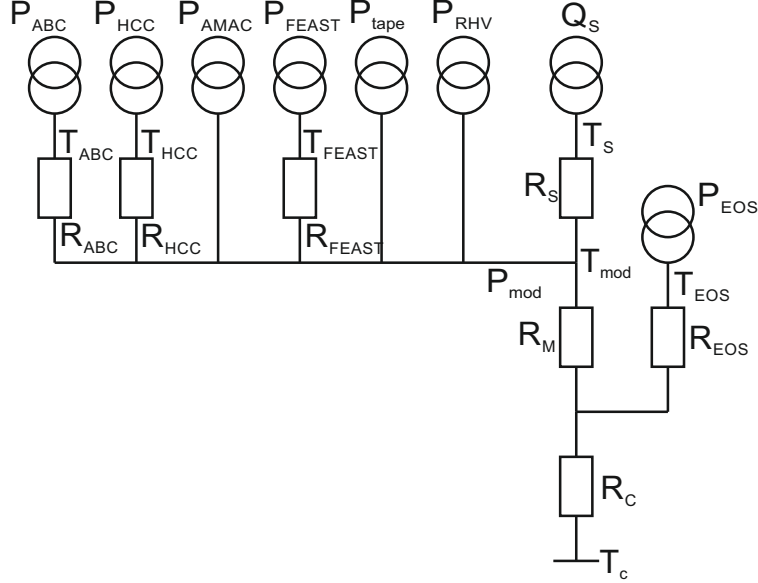


Figure 5: Thermal network model.

#### 4. Obtaining thermal impedances using FEA

Explain the method of extracting impedances of thermal pathways using FEA.

#### 5. Other model inputs

Explain the specific challenges in the strip detector that are parameterized and modeled in our case.

##### 5.0.1. DCDC converter

The DCDC converter (FEAST) supplies a low-voltage (1.5 V) current to the ABC130 and HCC front-end chips on the module. The efficiency of the FEAST depends on its temperature as well as the output (load) current load delivered to the front-end chips. To correctly model the FEAST efficiency, experimental measurements are performed to characterize the dependence and fitted with a functional form.

To measure the FEAST efficiency, the FEAST power board was glued to an aluminum cold plate, cooled with CO<sub>2</sub>, and powered with the nominal working input and output voltages (11 V input, 1.5 V output). The temperature of the FEAST is measured with an NTC thermistor and PTAT sensor residing on the FEAST, for a range of load currents up to the maximum design current of 4A<sup>1</sup>.

The data is then fit with a function with sufficient parameters to ensure reasonable agreement; the choice of functional form has no physical interpretation. Figure 6 depicts the FEAST efficiency data and the parameterized fit used in the model.

##### 5.0.2. Digital current increase of chips using 130 nm CMOS technology

The ABC and HCC chips, designed using IBM 130 nm CMOS8RF technology, are known to suffer from an increase in digital current when subjected to a high-radiation environment [2]. This phenomenon, known as the “TID bump,” is well-studied [3, 4] and has a characteristic shape whereby the effect reaches a maximum over a period of time and then gradually diminishes (see Fig. 7).

In an effort to characterize the nature of the TID bump in the ABC and HCC chips empirically, many irradiation campaigns have been conducted using a variety of radiation sources, testing the effect at different temperatures and dose rates. The data collected from these studies was used to develop a model of the

---

<sup>1</sup> FEAST data spreadsheet: [http://project-dcdc.web.cern.ch/project-dcdc/public/Documents/FEASTMod\\_Datasheet.pdf](http://project-dcdc.web.cern.ch/project-dcdc/public/Documents/FEASTMod_Datasheet.pdf). Cite?

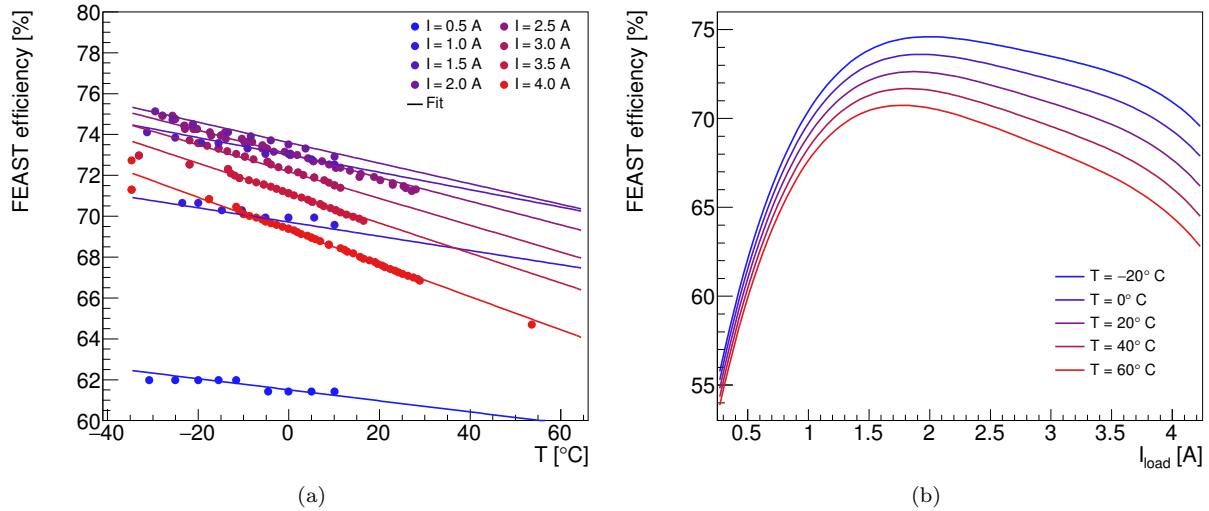


Figure 6: The FEAST efficiency model based on experimental data. (a) The experimental data points characterizing the FEAST efficiency are plotted as dots and color coded for load current. The data is compared to the analytic fit, evaluated in curves of equal current. (b) The same analytic fit, presented as a function of current load for curves of equal temperature.

TID bump that estimates the digital current increase given the total ionizing dose, the dose rate, and the operating temperature of the chip. This parameterization, which is depicted in Fig 7, is used as an input to the thermoelectric model in order to correctly model the ABC and HCC currents. The TID bump is assumed to fully apply to the HCC digital current, and apply to 69% of the ABC digital current (according to our understanding of its digital circuitry).

The TID bump displays certain key features, which are reflected in the parameterization: first, the effect is larger at colder temperatures and higher dose rates. This means it can be mitigated by operating the chips at higher temperature (note that the dose rate is fixed by the LHC conditions). Second, the figure also illustrates how chips receiving different dose rates will reach their maximum digital current increase at different times. This feature is particularly important when modeling the total power consumed by the barrel and endcap systems. In both systems, the dose rate varies significantly depending on the position of the module in the detector. The effect means that the maximum total power will be smaller than the sum of the maximum power of each module, as each chip reaches its maximum at a different point in time.

### 5.0.3. Modeling flux and total ionizing dose in endcap modules

Covered already in the introduction?

## 6. Running the model

The thermoelectric model constructs a profile of the sensor module operation conditions over the lifetime of the detector in the following manner. First, assuming a reasonable set of initial component temperatures, the module total power (including all components, but excluding the sensor leakage power) and the sensor temperature without leakage current ( $T_0$ ) is calculated assuming these initial temperatures. The initial value for the module power is used to solve for the sensor power and temperature accounting for leakage current, using the thermal balance equation and the relationship from Eq. ???. Using the calculated sensor leakage current and temperature, the power and temperature of the module components are updated given the initial (year-0, month-0) startup parameters.

Next, the module conditions of the following month (year-0, month 1) are calculated. Using the component temperatures calculated from the previous month and the operational parameters (ionizing dose and dose rates) from month 1, the module total power (excluding sensor leakage) is again recalculated, and subsequently the sensor temperature and leakage current are recomputed. Following this, the module component

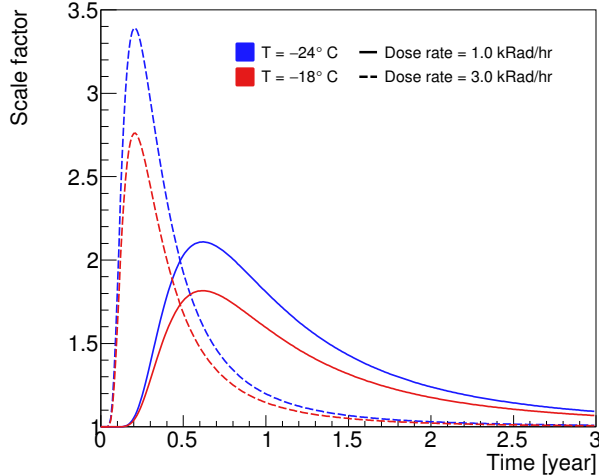


Figure 7: Parameterization of the impact of the total ionizing dose on the magnitude of the front-end chip digital current, as a function of time. The current is multiplied by a scale factor that is modeled as a function of total ionizing dose, dose rate, and temperature, based on experimental data.

temperatures and power values are updated. This process is repeated in one-month steps until the final year of operation, or until a real solution for the sensor temperature does not exist, indicating that thermal runaway conditions have been reached.

In the barrel subsystem, the above procedure is performed four separate times to represent the conditions of the four barrel layers located at different radii from the beam axis<sup>2</sup>. The procedure is also performed once for a module adjacent to an EOS and a representative module of the remaining 13 without an adjacent EOS. In each case, the worst-case total ionizing dose and dose rate is assumed for each layer, though these values are relatively consistent for a given layer. In total, 8 modules are simulated, and they are combined in their proper proportion to simulate the entire barrel system.

In the endcap subsystem, the total ionizing dose and dose rates vary significantly depending on the position of the module; furthermore, the design of each module on a petal differs significantly. Therefore, all 36 module types (6 rings × 6 disks) are simulated independently, and combined to represent the full endcap.

## 7. Outputs of the thermoelectric model

### 7.1. Operational scenarios

To study the different aspects of our predictions for the operation of the ITk strip system throughout its lifetime we performed the calculation of the system parameters over the expected 14 years of operation in monthly steps. Time-dependent inputs to the calculations were given from the expected performance of the LHC (figure 8a) and different profiles for the cooling temperature. We studied flat cooling temperature scenarios at different temperatures starting at -35°C, the lowest evaporation temperature achievable with the ITk evaporative CO<sub>2</sub> cooling system, and a ‘ramp’ scenario, where the cooling temperature starts at 0°C and gradually is lowered down to -35°C (figure 8b).

### 7.2. Safety factors

To ensure the robustness of the system design against errors in the assumptions used in the model we ran the model in addition to the nominal set of input parameters with a set where some key inputs have been degraded. The set of safety factors used are given in table 1. Each safety factor has been estimated individually based on experience, the complexity of the system aspect described by the parameter, and from available data or the absence of such data. Note that when the model was evaluated with safety factors all

---

<sup>2</sup> The correct module type, short-strip in the inner two layers and long-strip for the outer two layers, is used for each layer.

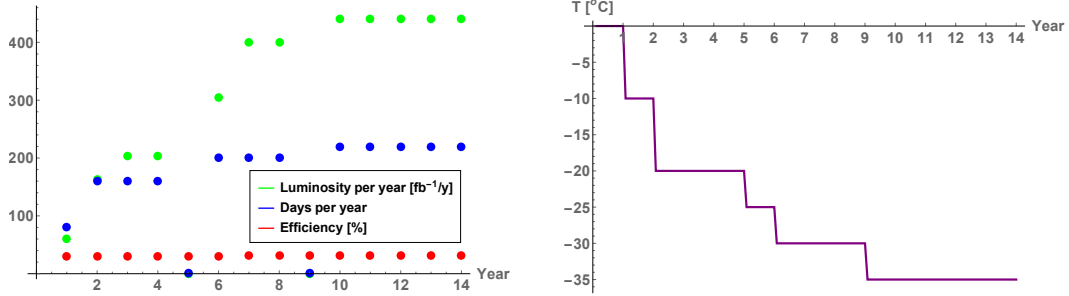


Figure 8: Expected LHC performance (left) and cooling ramp' scenario for the cooling temperatures (right). Year-long shutdowns of the LHC are anticipated in years 5 and 9.

the safety factors in table 1 were used together, a situation which is unlikely to occur in the real system, thus providing a worst case estimate for the performance of the ITk strip system.

Table 1: Safety factors.

Safety factor on	Value	Reason
Fluence	50%	Accuracy of fluence calculations and uncertainties in material distributions
Thermal impedance	10%	Local support build tolerances
Digital current	20%	Final chip performance and parametrization of TID effect
Analog current	5%	Final chip performance
Tape impedance	10%	Electrical tape manufacturing tolerances
Bias voltage	700 V	Increased bias voltage from 500 V to maintain S/N
TID parametrization	Nominal/Pessimistic	Different data sets for fit of TID bump

### 7.3. Results

The thermo-electrical model provides a large range of predictions for the operation of the strip system. A detailed discussion of all results would only be of interest for ITk strip community members and is beyond the scope of this article. Instead we will present here a subset of results to demonstrate the capabilities and use of the thermo-electrical model for the design of the detector system.

#### 7.3.1. Module properties

Some example output plots for module properties from the thermo-electrical modules are shown in figures 10 and 14. The different radiation-dependent effects occur on different times scales. The maximum in the digital chip power due to the TID effect occurs relatively early (in year 1 to 4), although the bump has a long tail, particularly in the outer layers of the barrel. The sensor leakage power on the other hand grows towards the end of the lifetime of the ITk. Due to the radius-dependence of the radiation environment the radiation-induced effects are most pronounced in the innermost layer.

#### 7.3.2. System properties

One of the key concerns for the design of the strip system is thermal stability of the system. If the cooling temperature is too high to limit the leakage power from the radiation-damaged sensors to a level where it can still be removed the system is unstable (it goes into ‘thermal runaway’). In this case there is no solution to the set of equations in the thermo-electrical model any more and the numerical search for a solution fails. In the barrel strip system this happens in the last year of operation at a cooling temperature of -15°C under nominal conditions, and at -25°C (in year 13) with safety factors applied. As the design cooling temperature of the ITk cooling system is -35°C we have confidence that the ITk strip system has sufficient margin for thermal stability.

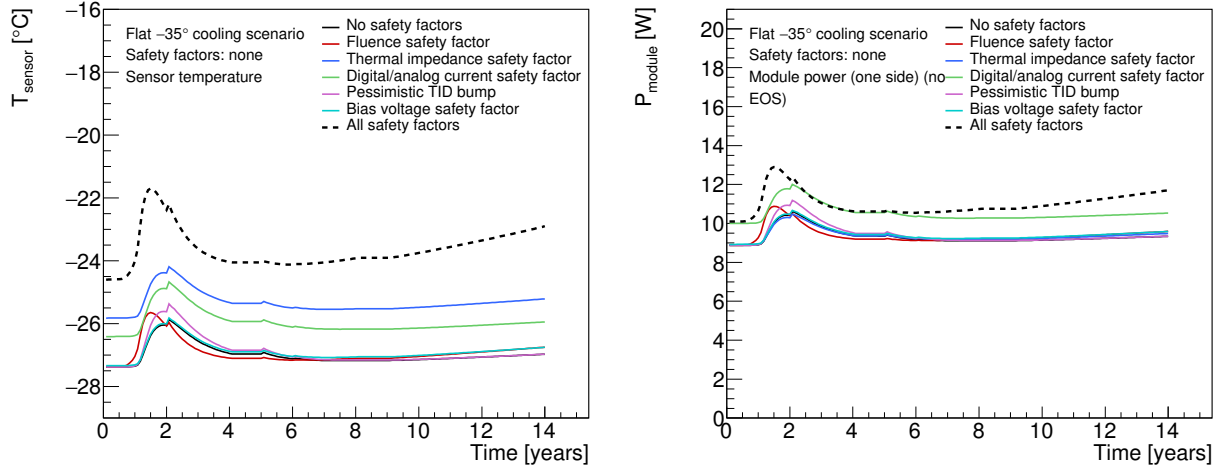


Figure 9: Comparing the impact of different safety factors.

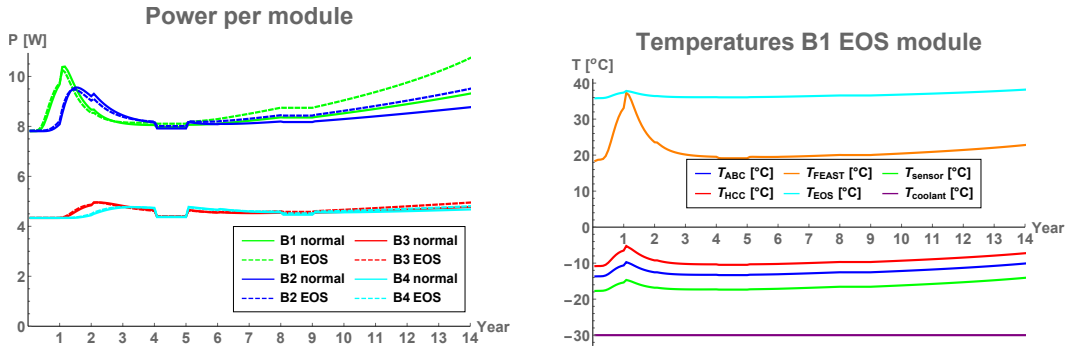


Figure 10: Examples for barrel module performance predictions for a flat cooling scenario ( $-30^\circ$ ) including safety factors. Power per module (left). Temperatures for different parts of and end-of-stave barrel module in the innermost barrel (right).

Beyond the issue of stability, the thermo-electrical model delivers predictions for the development of current and power requirements for the overall system. Some of the predictions are shown in figure 12. Ignoring this time dependence could lead to overspecification of the cooling system.

These predictions are now used throughout the strip project to consistently size power supply and cooling systems. Including safety factors in the predictions gives us some confidence that the designs are robust and by using commonly agreed safety factors we ensure a consistent use of safety factors throughout the project and prevent safety factor creep.

Because of the different timescales for the peak power due to the TID effect and the sensor leakage due to radiation there is room for the optimization of the cooling temperature profile for minimal power. The thermo-electrical model is a powerful tool to plan such an optimized cooling profile. In fact, the cooling ‘ramp’ scenario introduced in section 7.1 is the result of such an optimization (figure 13).

## 8. Model performance verification

The quality of the predictions of the thermo-electrical model is affected by two major factors: First, there is the quality of the input parameters, and second there are errors introduced by reducing the complex 3D geometry into a linear thermal impedance network. The former have been discussed throughout this paper where the different inputs have been presented. For the latter we have studied the agreement of predictions from network model with the more accurate results obtained from FEA for selected states of the system.

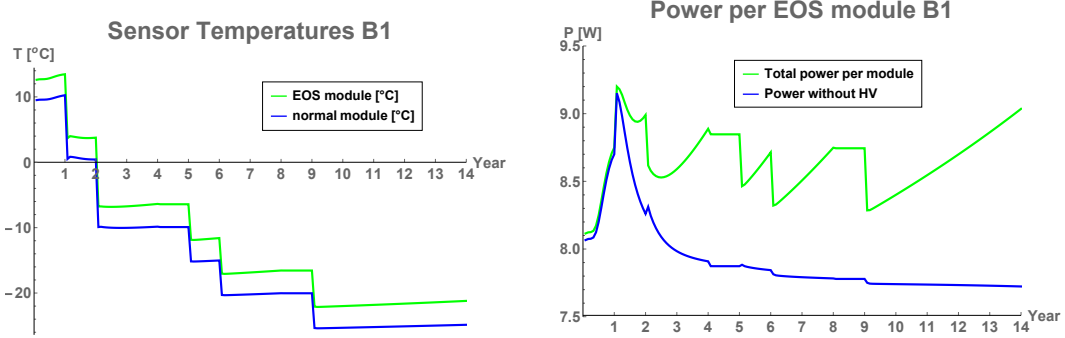


Figure 11: Examples for barrel module performance predictions for the ramp cooling scenario including safety factors. Temperature in innermost barrel modules (left). Power in an end-of-stave barrel module in the innermost barrel (right).

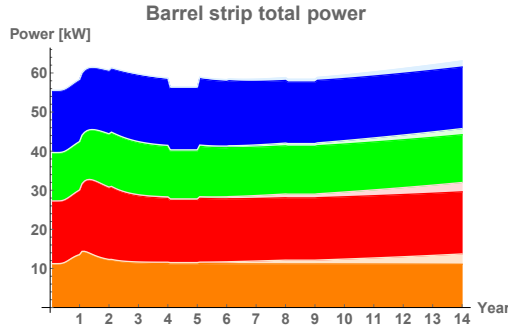


Figure 12: Examples for system performance predictions. Barrel total power requirements for flat  $-30^\circ$  cooling including safety factors (left): The plot shows the stacked power requirements for the four barrels (orange: innermost barrel, blue: outermost barrel). The greyed parts are contributions from HV power for the four barrels.

For the verification of this agreement we have studied the sensor temperature curve for a barrel end-of-stave module up to thermal runaway. For this study we do not vary any of the input parameters in the model other than the sensor leakage power. We therefore can reduce the complex network to its Thevenin equivalent, which is identical to the network studied in ref. [1] and we use the analytical expressions given there. The comparison of this prediction is shown in figure xxx. Despite a large temperature variation of about  $15^\circ\text{C}$  across the sensor, which is caused by heat flux from the end-of-structure card and degraded thermal impedance at the end of the stave due to ceramic sections in the cooling pipe, the network model predicts the runaway within  $1^\circ\text{C}$  of the result from the FEA. This agreement is not likely to significantly degrade the predictions beyond the errors introduced by uncertainties of other inputs to the model.

## 9. Conclusions

(Conclusions.)

## 10. Acknowledgements

(Acknowledgements.)

## References

- [1] G. Beck, G. Viehhauser, Analytic model of thermal runaway in silicon detectors, Nucl. Instrum. Meth. A618 (2010) 131–138. doi:10.1016/j.nima.2010.02.264.

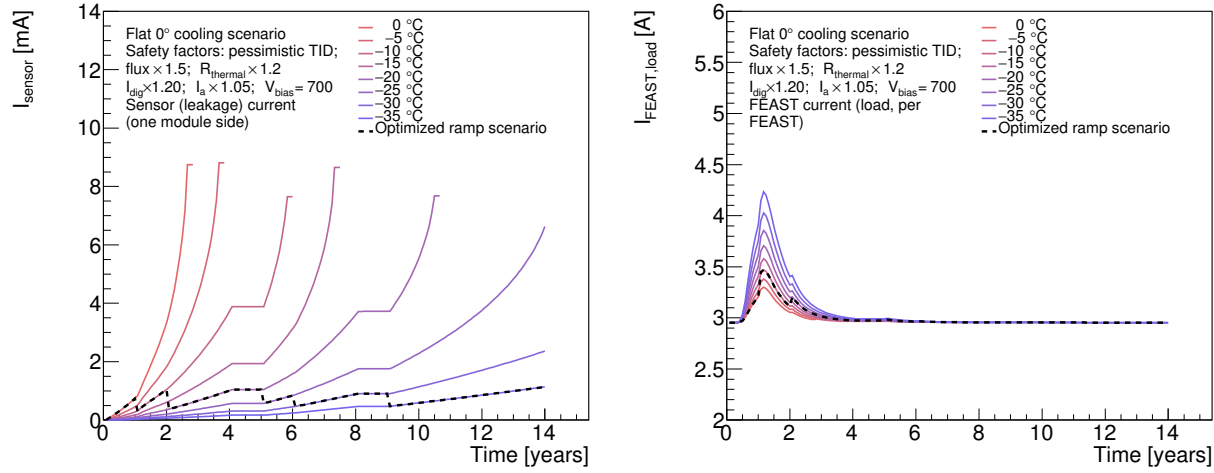


Figure 13: Optimization of the cooling ‘ramp’ scenario. The dashed lines represents the ramp scenario, which has been selected so that the sensor leakage current is stable throughout the lifetime of the ITk (left). The higher cooling temperatures in the first years keep the TID effect relatively small (right).

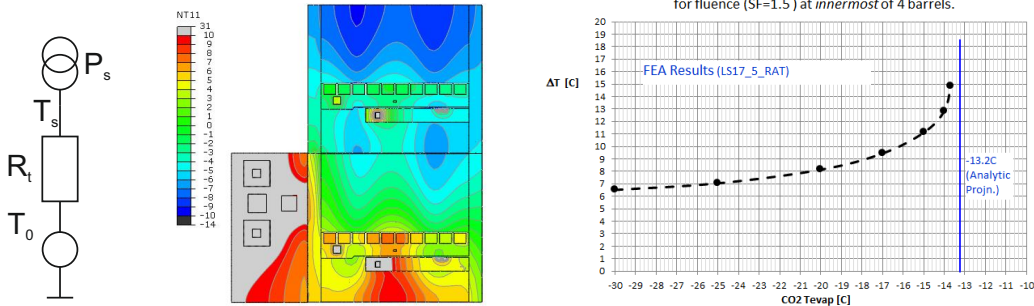


Figure 14: Thevenin equivalent of the thermal network (left). Result of surface temperature calculations using FEA (middle). Average temperature above cooling - comparison between FEA (dots) and network model prediction (right).

- [2] ATLAS Collaboration, Technical Design Report for the ATLAS Inner Tracker Strip Detector.
- [3] F. Faccio, G. Cervelli, Radiation-induced edge effects in deep submicron cmos transistors, IEEE Transactions on Nuclear Science 52 (6) (2005) 2413–2420. doi:10.1109/TNS.2005.860698.
- [4] F. Faccio, H. J. Barnaby, X. J. Chen, D. M. Fleetwood, L. Gonella, M. McLain, R. D. Schrimpf, Total ionizing dose effects in shallow trench isolation oxides, Microelectronics Reliability 48 (7) (2008) 1000 – 1007, 2007 Reliability of Compound Semiconductors (ROCS) Workshop. doi:<https://doi.org/10.1016/j.microrel.2008.04.004>.  
URL <http://www.sciencedirect.com/science/article/pii/S0026271408000826>